

Achieving superior ductility with ultrahigh strength via deformation and strain hardening in the non-recrystallized regions of the heterogeneous-structured high-entropy alloy

Hongchao Li ^{a,b}, Jun Wang ^{a,*}, Wenyuan Zhang ^a, Jiawang Zhao ^a, Jinshan Li ^a, M.W. Fu ^{b,*}

^a State Key Laboratory of Solidification Processing, School of Materials Science and Engineering, Northwestern Polytechnical University, Xi'an 710072, PR China

^b Department of Mechanical Engineering, Research Institute for Advanced Manufacturing, The Hong Kong Polytechnic University, Hung Hom, Kowloon, Hong Kong, PR China



ARTICLE INFO

Keywords:

High-entropy alloys
Heterogeneous-structured
L₁₂ strengthening
Transformation-induced plasticity
Non-recrystallized regions

ABSTRACT

Developing metallic structural materials with ultrahigh strength and exceptional ductility remains a significant challenge due to the trade-off between both properties. This study presents a heterogeneous-structured high-entropy alloy achieving a superior combination of strength and ductility compared to the reported heterogeneous-structured high entropy alloys through deformation and strain hardening in the non-recrystallized regions. The cold rolling followed by annealing at 760 °C resulted in a heterogeneous microstructure consisting of a small fraction of ultrafine recrystallized grains and extensive non-recrystallized regions, with a significant amount of L₁₂ precipitates throughout the alloy. The architected microstructure led to a significant enhancement of yield strength through mechanisms including dislocation strengthening, L₁₂ strengthening, and grain boundary strengthening. During the deformation, the non-recrystallized regions accommodated substantial strain through the reactivation of pre-existing deformation bands and the synergistic deformation of the FCC and L₁₂ phases, thereby markedly enhancing ductility. Moreover, the metastable FCC matrix underwent FCC→BCC phase transformation, leading to the formation of numerous short-range BCC domains, which further contributed to the pronounced strain hardening. Consequently, the alloy annealing at 760 °C achieved a yield strength of 1.73 GPa, an ultimate strength of 2.05 GPa, and an elongation of 21.0 %. This study underscores a novel strategy for the concurrent enhancement of strength and ductility and provides valuable insights for the design of high-performance alloys.

1. Introduction

Metallic structural materials with ultrahigh strength and ductility are essential for advanced industries like aerospace, automotive manufacturing, and energy production. These materials play a critical role in ensuring superior energy efficiency and reliability in demanding engineering applications. Unfortunately, due to the inverse relationship between strength and ductility, most strengthening mechanisms increase alloy strength at the expense of the ability to undergo further strain hardening after yielding [1–3]. Alloys with ultrahigh strength (ultimate tensile strength \geq 2 GPa) often exhibit low ductility, typically <10 % [4,5]. This significantly affects their processing performance and can lead to catastrophic failure during service. For example, nanocrystalline metallic materials exhibit high hardness and strength due to

the Hall-Petch effect [1]. Despite their high strength, these materials suffer from limited ductility because their fine-grained structure suppresses deformation mechanisms based on full-dislocation motion and grain boundary activities [6–8]. Numerous defects, such as dislocations, stacking faults and twins, which can be introduced by cold working, are highly effective for strengthening alloys. Yet, this method usually results in significant ductility loss, as it sacrifices strain hardening capacity due to premature dislocation accumulation and stress concentration [9,10]. Transformation-induced plasticity (TRIP) can significantly enhance strain hardening in alloys, leading to superior tensile strength and ductility. Nonetheless, these alloys typically exhibit reduced yield strength owing to a significant proportion of soft phases in their initial microstructure [11–13]. Although coherent precipitation strengthening can increase yield strength with minimal sacrifice in tensile ductility, the

* Corresponding authors.

E-mail addresses: nwpwuj@nwpu.edu.cn (J. Wang), mmmwfu@polyu.edu.hk (M.W. Fu).

overall improvement in strength is limited [14,15]. Recently, heterogeneous microstructures have been developed to balance alloy strength and ductility by enabling the cooperative deformation of coarse grains or soft phases with fine grains, non-recrystallized grains, or hard phases [16]. Nevertheless, achieving a high strength-ductility combination with this method often necessitates sacrificing some strength or ductility [2, 17]. In particular, alloys with recrystallized (RX) and non-recrystallized (NRX) regions generally show reduced strength compared to rolled alloys primarily due to recovery and recrystallization [18–20]. Their ductility is also inferior to fully recrystallized alloys because the non-recrystallized regions cannot effectively accommodate deformation [19,21]. Therefore, developing high-performance alloys with ultrahigh strength and ductility remains challenging, which requires the synergistic action of various strengthening mechanisms to overcome individual limitations.

Recently, multicomponent high-entropy alloys (HEAs) have garnered considerable research interest because their innovative compositional design offers a wide range of options for tuning microstructures and applying strengthening methods [22–24]. Obviously, HEAs provide greater flexibility in achieving compositions that integrate multiple strengthening mechanisms compared to traditional alloys with a single-component design concept [25,26]. In our previous work, we found that increasing Fe content promotes transformation from the face-centered cubic (FCC) phase to the body-centered cubic (BCC) phase in L₁₂-strengthened Al₅Ti₈(FeCoNi)_{86.9}B_{0.1} HEAs during tensile deformation, thereby enhancing strain hardening and optimizing the combination of strength and ductility [27]. Based on this, we increased the Fe content to 29 % to further amplify the transformation-induced plasticity effect. This adjustment led to the creation of a new model alloy, Al₅Ti₈(FeCoNi)_{86.9}B_{0.1} HEA.

Therefore, in this study, we engineered a heterogeneous microstructure primarily consisting of NRX regions, along with limited RX areas with ultrafine grains, by cold rolling and annealing the Al₅Ti₈(FeCoNi)_{86.9}B_{0.1} HEA within the FCC+L₁₂ two-phase region. Numerous nano-scaled L₁₂ particles formed in the RX and NRX regions significantly improve alloy strength. The NRX regions accommodated significant deformation through the activation of deformation bands, contributing to the high ductility. A metastable FCC matrix was formed around the L₁₂ precipitates and underwent FCC→BCC transformation during deformation, thereby enhancing both strain hardening and ultimate strength. Consequently, the alloy annealed at 760 °C retains an exceptional strength-ductility synergy with an ultimate strength of 2.05 GPa and ductility of 21.0 %. This novel strategy, involving deformation and strain hardening in the non-recrystallized regions, not only elevates the mechanical properties to remarkable levels but also offers a robust solution to the challenge of achieving an optimal strength-ductility balance in advanced materials.

2. Materials and methods

2.1. Alloy design and fabrication

The Al₅Ti₈(FeCoNi)_{86.9}B_{0.1} HEA was developed by incorporating an additional one at % of Fe into the existing Al₅Ti₈Fe₂₈(CoNi)_{58.9}B_{0.1} HEA, based on our prior research [27]. The corresponding phase diagram is presented in Fig. 1. The volume fraction of boride (MB₂) in the solid phase region is approximately 0.15 % and is therefore considered negligible. The FCC single-phase region of the HEA, located between 1108 and 1228 °C, allows for the selection of homogenization and recrystallization annealing temperatures to ensure the formation of a single FCC phase. The FCC + L₁₂ two-phase region spans 742 to 871 °C, where annealing is conducted to promote the precipitation of the L₁₂ phase within the FCC matrix.

The ingots of Al₅Ti₈(FeCoNi)_{86.9}B_{0.1} (at. %) HEA were fabricated from metals with purity exceeding 99.9 wt.% in a vacuum arc melting furnace. Each ingot underwent five remelting cycles to ensure chemical

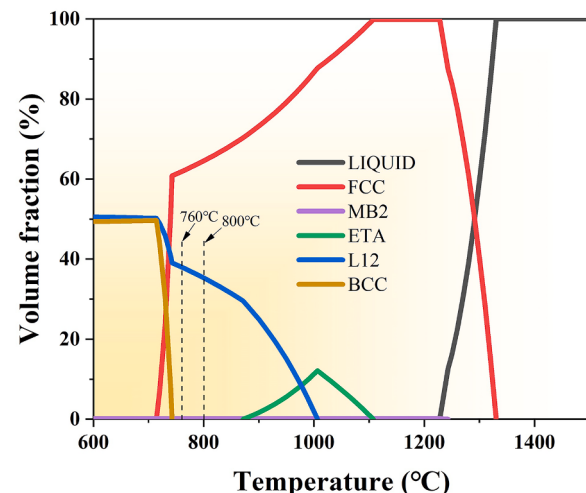


Fig. 1. Phase diagram of Al₅Ti₈(FeCoNi)_{86.9}B_{0.1} HEA calculated using JMatPro software and NiFe-based superalloy database.

homogeneity before being cast into a water-cooled copper mould measuring 50 × 15 × 10 mm³. Subsequently, the cast ingots were homogenized at 1200 °C for two hours and then subjected to multi-pass rolling at room temperature to achieve a 50 % reduction in thickness (from 10 mm to 5 mm). Following rolling, the samples were heat-treated at 1165 °C for 10 min to achieve a recrystallized FCC-type grain microstructure (abbreviated as HT alloy). Afterwards, the samples underwent further multi-pass rolling to achieve an 80 % reduction in thickness (from 5 mm to 1 mm), abbreviated as the CR alloy. The cold-rolled samples were then annealed in the FCC+L₁₂ two-phase region (Fig. 1) at 760 and 800 °C for two hours and were designated as CR760 and CR800 alloys, respectively. All heat treatments were followed by quenching in water.

2.2. Microstructure characterization

The phase composition of the alloys was analyzed using a Bruker D8 DISCOVER A25 X-ray diffractometer (XRD). Measurements were performed using Co K α radiation ($\lambda = 0.179021$ nm) over a range of 20° to 130° with a scanning step of 0.02°. Before XRD testing, the sample surface was polished using 2000-grit SiC paper. Scanning electron microscopy (SEM), electron backscattered diffraction (EBSD), and transmission Kikuchi diffraction (TKD) observations were conducted to characterize the microstructure using a Tescan Amber SEM equipped with an automatic orientation acquisition system (Oxford Instrument, Symmetry S2). The SEM and EBSD samples were prepared by mechanically ground and then electropolished at 5 °C in an electrolyte containing 90 % ethanol and 10 % perchloric acid. Transmission electron microscopy (TEM) was performed for further characterization of second phases and deformed microstructure on a Tecnai F30 G2 microscope and a Talos F200X instrument equipped with a four-probe high-resolution energy dispersive spectroscopy (EDS) system. TKD and TEM samples were initially mechanically grounded to a uniform thickness of 50–60 μ m using 2000-grit sandpaper and subsequently punched into 3 mm diameter discs. For the deformed samples, thin slices measuring 4 × 2 × 0.5 mm³ were cut from the gauge section of the deformed tensile specimens using electrical discharge machining (EDM). These slices were ground to a thickness of 50–60 μ m using 2000-grit sandpaper and mounted on molybdenum grids. The final thinning of the samples was achieved using a double-jet electropolisher at an applied voltage of 25 V and a temperature of –25 °C.

2.3. Mechanical properties test

Tensile specimens with a dog-bone shape, featuring an 8 mm gauge length and a $2 \times 1 \text{ mm}^2$ cross-sectional area, were prepared using EDM along the rolling direction of the material. Uniaxial tensile tests were conducted at room temperature using a Zwick Roell Z5.0TN electronic testing machine. The real-time strain of the tensile specimens was recorded using a Zwick Roell 1–15 HP laser extensometer with a tensile strain rate of $1 \times 10^{-3} \text{ s}^{-1}$. At least three samples were tested to ensure data reproducibility. Additionally, loading-unloading-reloading (LUR) cyclic tests were conducted on the tensile specimens to evaluate long-range residual stress and short-range effective stress during deformation. This approach enabled the characterization of hysteresis curves reflecting the alloy Bauschinger effect. The unloading strain increment

was set at 2 %. The tensile specimens were initially loaded at a rate of $1 \times 10^{-3} \text{ s}^{-1}$ to a specific strain, followed by unloading to 20 N at a rate of 2000 N/min, and then reloaded to initiate the next cycle.

2.4. Strain partitioning measurement by micro-digital image correlation (μ -DIC)

Quasi-in-situ μ -DIC was performed using tensile specimens to analyze strain distribution during deformation. After electropolishing, a gold film was coated on the gauge section of the specimen surface using a vacuum sputter coater. The specimens were then placed in a vapour deposition apparatus and heated to 280 °C for approximately two hours. This process resulted in uniformly distributed gold particles on the specimen surface, serving as speckles for DIC analysis. Tensile loading

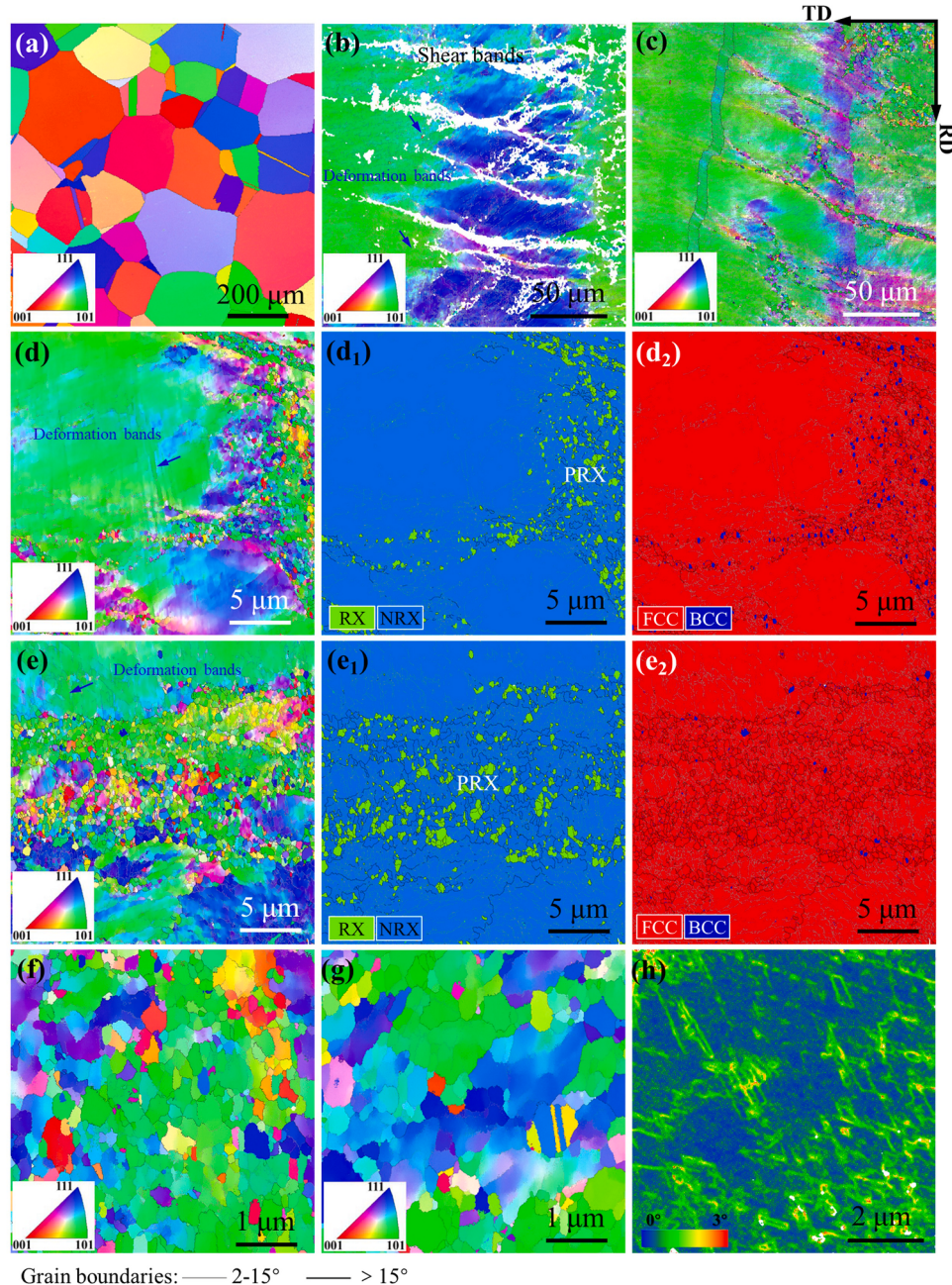


Fig. 2. Microstructures of the $\text{Al}_5\text{Ti}_8(\text{FeCoNi})_{86.9}\text{B}_{0.1}$ HEA after different processes by EBSD and TKD characterization. IPFs of HT (a), CR (b), and CR760 (c) alloys. Enlarged IPFs, distribution maps of RX and NRX regions, as well as phase distribution maps in CR760 (d) and CR800 (e) alloys. Magnified views of RX regions in CR760 (f) and CR800 (g) alloys. (h) TKD KAM map of the NRX region in CR760 alloy.

and unloading were conducted using a Kammrath & Weiss micro-test system equipped with a 5 kN load cell at a strain rate of $5 \times 10^{-4} \text{ s}^{-1}$. Upon reaching a defined strain, unloading was performed using the same strain rate, and the alloy deformation after unloading was recorded. Backscattered electron images at various deformation stages were captured after unloading with a resolution of 2048×2048 pixels ($8 \times 8 \mu\text{m}^2$ field of view). For data analysis, Ncorr v1.2 software was used to create surface components, setting the subset radius for DIC analysis to 15×15 pixels and the spacing to 2 pixels. Finally, micro-strain partitioning maps were generated at different strain levels.

3. Results

3.1. Heterogeneous microstructures achieved by partial recrystallization

Figs. 2a-c display the inverse pole figures (IPFs) of the TD-RD sections for HT, CR and CR760 alloys. The microstructure of the initial HT alloy comprises randomly oriented FCC recrystallized grains (Fig. 2a). After multiple rolling passes, the CR alloy exhibits elongated grains along the TD direction. These deformed grains are intersected by several macroscopic shear bands and exhibit a significant number of deformation bands within the grain interior (Fig. 2b). Annealing at 760°C for two hours results in a small fraction of RX regions within the shear bands (Fig. 2c). Figs. 2d and e present the magnified IPF maps of CR760 and CR800 alloys, along with the corresponding distribution maps of recrystallized grains (mean grain orientation spread (GOS) $< 2^\circ$) and phases. Increasing the annealing temperature from 760°C to 800°C led to an increase in the recrystallization volume fraction. For CR760 and CR800 alloys, the recrystallization volume fractions were determined by randomly selecting multiple regions, resulting in 7.3 % and 9.8 %, respectively. Notably, surrounding the recrystallized grains are numerous sub-grains with a mean GOS larger than 2° , which, along with the recrystallized grains, constitute partially recrystallized (PRX) regions in the CR760 and CR800 alloys, as shown in Fig. 2d₁ and e₁. The phase distribution maps (Fig. 2d₂ and e₂) reveal that a small fraction of

the BCC phase emerged in the RX regions after annealing, and the BCC phase volume fractions in the CR760 and CR800 alloys were determined to be 1.2 % and 0.6 %, respectively. Analysis of the enlarged view of the RX region reveals that the average recrystallized grain sizes are approximately $0.16 \mu\text{m}$ for CR760 alloy (Fig. 2f) and $0.22 \mu\text{m}$ for CR800 alloy (Fig. 2g). It should be noted that the deformed bands in the NRX regions remained after annealing compared with the CR sample (Fig. 2b-e). A detailed TKD analysis was conducted to examine the distribution and misorientation of the deformed microstructure in the CR760 alloy. As depicted in Fig. 2h, the kernel average misorientation (KAM) map reveals significant orientation disparities (approximately $1^\circ - 3^\circ$) across the deformation bands.

3.2. Phase precipitation in the heterogeneous microstructure

Fig. 3a shows the XRD patterns depicting the phase compositions of CR, CR760, and CR800 alloys. The XRD pattern of CR alloy reveals that it consists of a single FCC phase. After annealing at 760 and 800°C for two hours, a weak (110) diffraction peak attributed to the L₁₂ phase at approximately 41° , indicating L₁₂ phase formation in the alloys. Additionally, the weak (110) diffraction peak of the BCC phase is observed near 52° in the XRD patterns of the CR760 and CR800 alloys, suggesting the presence of a minor amount of BCC phase.

The microstructure and phase composition of CR760 and CR800 alloys were further analyzed using SEM, as shown in Fig. 3b-f. Both PRX and NRX regions of the alloys exhibit distinct contrasts under secondary electron conditions (Fig. 3b, d). In the NRX regions, abundant nanoscale precipitates are uniformly distributed, with their size increasing with increasing annealing temperature (Fig. 3c and e). Based on XRD analysis, these precipitates are inferred as the L₁₂ phase. In the recrystallized regions, two phases with different morphologies are observed: one appearing dark with a higher volume fraction and the other appearing white with a lower volume fraction, as shown in Fig. 3c and f. Given that Fig. 2d₂ and e₂ indicate the presence of a small amount of the BCC phase. The lighter phase is identified as BCC.

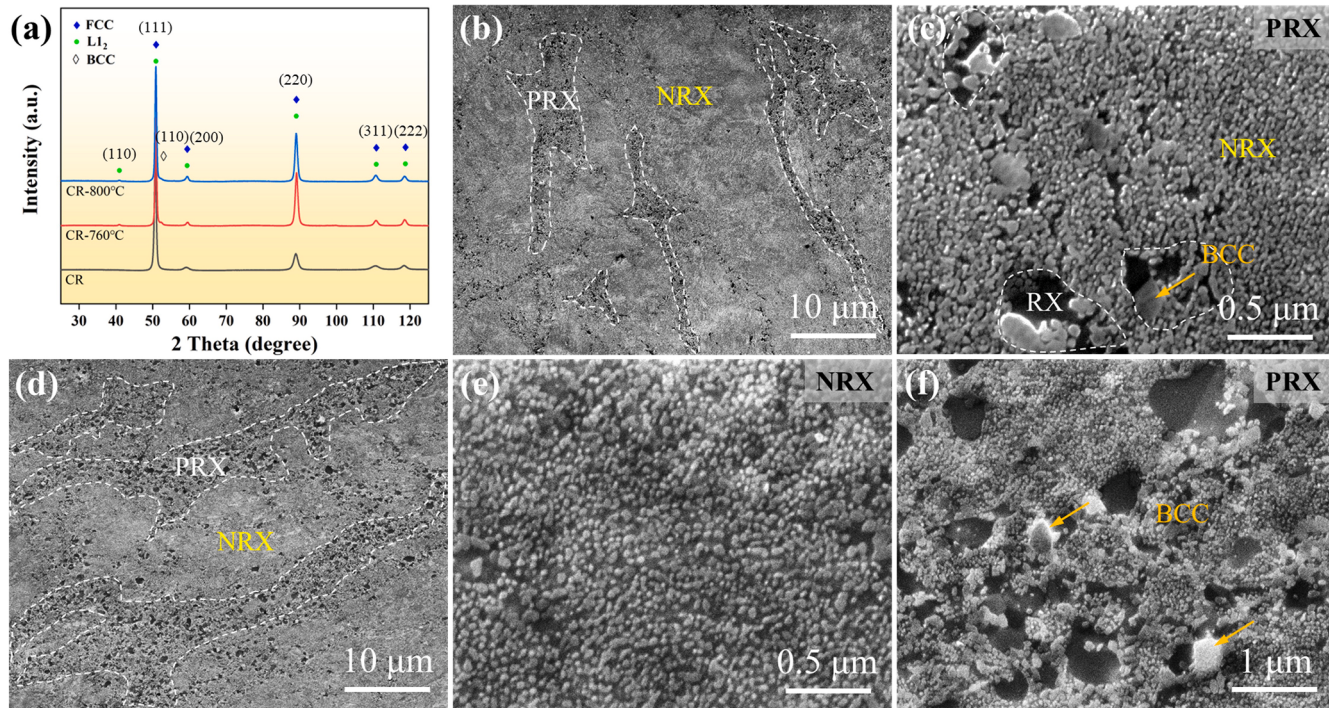


Fig. 3. Precipitated phases in RX and NRX regions. (a) XRD patterns of CR, CR760, and CR800 alloys. Microstructure of the CR760 alloy: (b) PRX and NRX regions. (c) Precipitate morphology in RX and NRX regions. Microstructure of the CR800 alloy: (d) PRX and NRX regions. (e) Precipitate morphology in NRX region. (f) Precipitate morphology in PRX region.

Fig. 4 presents the microstructural morphology of the CR760 and CR800 alloys as characterized by TEM. The bright-field TEM (BF-TEM) images (**Fig. 4a, b**) reveal band-like deformation structures extending in a single direction or two directions in the NRX region. The inset in **Fig. 4a**, showing two sets of selected area electron diffraction (SAED) spots obtained along the $\langle 110 \rangle$ axis, illustrates the different orientations between the deformation bands and the matrix. **Fig. 4c** displays a BF-TEM image of the recrystallized region, and the polycrystalline rings observed in the SAED pattern indicate the formation of randomly oriented recrystallized grains with nano sizes. The dark-field TEM (DF-TEM) image (**Fig. 4d**) confirms the L₁₂ structure of the precipitates (with sizes approximately 20–30 nm) in the NRX region. Smaller L₁₂ precipitates were observed within the FCC recrystallized grains (**Fig. 4e**). The high-resolution TEM (HR-TEM) image and the corresponding fast Fourier transform (FFT) pattern in **Fig. 4f** reveal a highly coherent interface between FCC and L₁₂ phases in NRX region, consistent with the reported precipitation of L₁₂ phase in recrystallized grains [28,29]. Additionally, the CR800 alloy exhibits similar microstructural features, as shown in **Fig. 4g-i**.

Fig. 5 presents a high-angle annular dark-field scanning transmission electron microscopy (HAADF-STEM) image alongside the corresponding

EDS map in the NRX region. The elemental compositions of the L₁₂ phase and FCC matrix are presented in **Table 1**. By combining the data from **Table 1** and **Fig. 5**, it is evident that the Ni-, Al-, and Ti-rich L₁₂ particles are uniformly distributed within the matrix and are unaffected by deformation bands or dislocation distribution. This is because the high coherence between the L₁₂ phase and the FCC matrix promotes uniform nucleation of the L₁₂ phase within the matrix, which is also observed in various HEAs with heterogeneous microstructures [30,31]. Additionally, the L₁₂ phase volume fractions in the NRX regions of the CR760 and CR800 alloys are approximately 45.4 % and 44.7 %, respectively. These values were determined using the lever rule, as detailed in the relevant studies [27,32].

3.3. Tensile properties

Fig. 6a displays the tensile stress-strain curves for the HT, CR, CR760, and CR800 alloys. The HT alloy exhibited a yield strength (YTS) of 0.87 ± 0.02 GPa and an ultimate strength (UTS) of 1.17 ± 0.03 GPa, accompanied by an elongation of $24.5\% \pm 1.3\%$. After cold rolling at room temperature, the CR alloy achieved yield strength and ultimate strength of 1.72 ± 0.02 GPa and 1.88 ± 0.02 GPa, respectively, with a limited

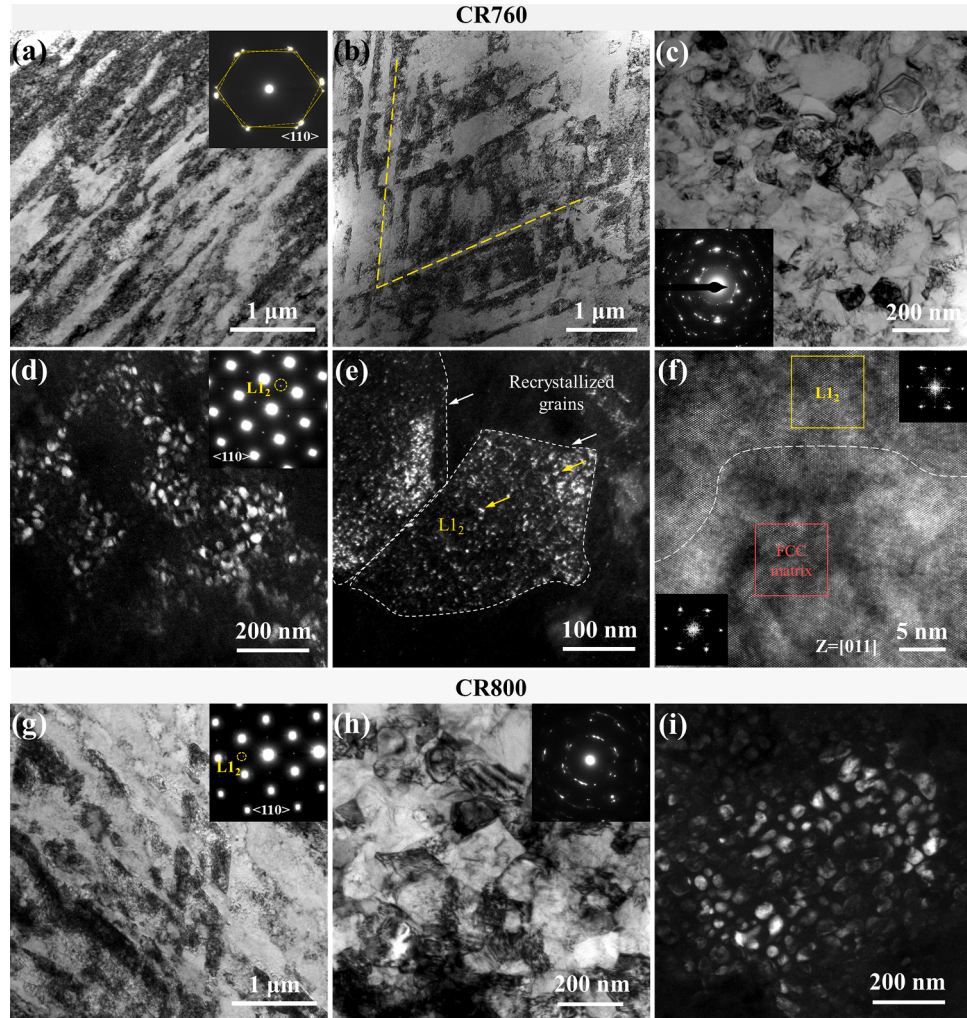


Fig. 4. Nanoscale microstructure of CR760 and CR800 alloys detected by TEM. CR760 alloy: (a, b) BF-TEM images of the NRX region show deformation bands and high-density dislocations, the inset in (a) is the corresponding SAED pattern. (c) BF-TEM image of the RX region, with the corresponding SAED pattern shown in the inset. (d) and (e) are the DF-TEM images of the L₁₂ phase in the NRX region and RX region, respectively, and the inset in (d) is the corresponding SAED pattern. (f) HR-TEM image at the interface between the L₁₂ phase and FCC matrix, with the corresponding FFT pattern located on the corners of the image. CR800 alloy: (g) BF-TEM image and corresponding SAED pattern of the NRX region. (h) BF-TEM image and corresponding SAED pattern of the RX region. (i) DF-TEM of the L₁₂ phase in the NRX region.

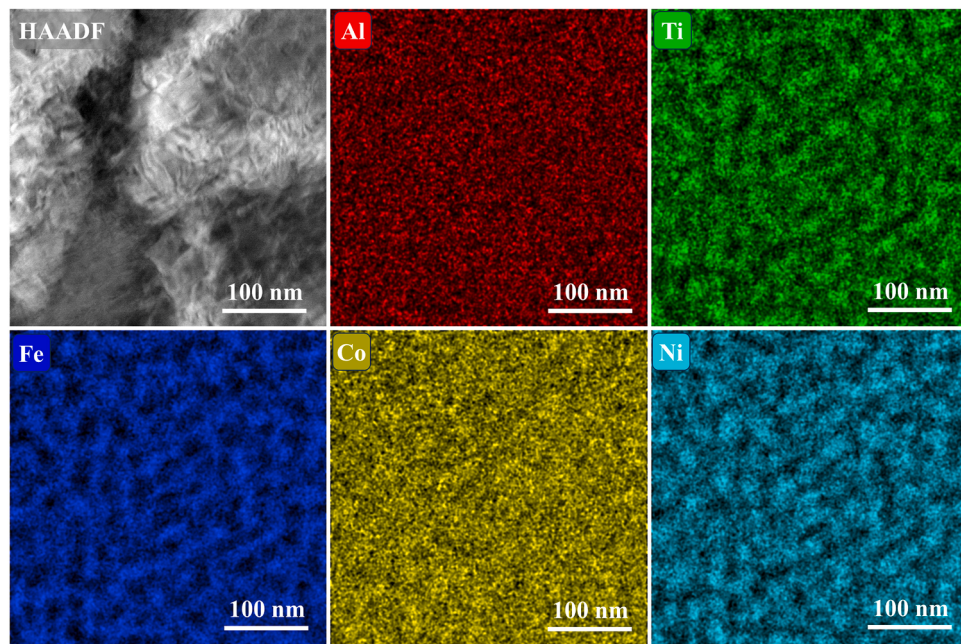


Fig. 5. HAADF-STEM image and corresponding EDS map of the NRX region in CR760 alloy, showing dense dislocation distribution and uniformly distributed L₁₂ precipitates.

Table 1

Elemental compositions of the L₁₂ precipitates and FCC matrix in the NRX region of CR760 and CR800 alloys, as detected by STEM-EDS.

Alloys	Phases	Compositions (at. %)					<i>f</i>
		Al	Ti	Fe	Co	Ni	
CR760	matrix	2.79	2.89	40.73	33.06	20.52	45.4 %
	L ₁ ₂	5.12	12.80	16.58	26.07	39.43	
CR800	matrix	2.26	4.12	39.25	32.23	22.14	44.7 %
	L ₁ ₂	3.38	11.54	19.17	27.88	38.03	

elongation of $5.0\% \pm 0.4\%$. The high yield strength and low elongation are attributed to substantial internal stress concentrations within the alloy. The CR800 alloy exhibited a yield strength of 1.57 ± 0.02 GPa, an ultimate strength of 1.76 ± 0.03 GPa, and an elongation of $16.3\% \pm 1.2\%$. This is encouraging, as the elongation nearly tripled with only a minor reduction in yield strength. Notably, after annealing at 760°C , the CR760 alloy achieved a yield strength of 1.73 ± 0.01 GPa, an ultimate strength of 2.05 ± 0.02 GPa, and an elongation of $21.0\% \pm 1.1\%$. This indicates that the yield strength is comparable to that of the CR sample, while the tensile ductility reached the level of the HT sample.

Notably, the tensile stress-strain curve for the CR800 alloy indicates necking at approximately 7 % strain, followed by a rapid strength decline. In contrast, the CR760 alloy maintains high uniform elongation after yielding. The work-hardening rate versus true strain curves for both alloys are depicted in Fig. 6b. During deformation, the work-hardening rate of the CR800 alloy initially drops rapidly, leading to premature necking at the true strain of 6.2 %. The work-hardening of the CR760 alloy proceeds in three stages: an initial rapid decrease, followed by a gradual increase, and finally, a slow decline. It maintains a high work-hardening rate even at large strains (up to a true strain of 16.2 %), contributing to its high uniform elongation and ultrahigh strength.

To highlight the superior mechanical properties of the heterogeneous-structured alloys in this study, we compared their tensile properties with those of other high-performance HEAs featuring heterogeneous microstructure (Fig. 6c and d). Our heterogeneous-structured HEAs, especially the CR760 alloy, exhibit exceptional strength (YTS and UTS) and significantly enhanced overall mechanical

performance compared to other heterogeneous-structured FCC, precipitation-hardened FCC, and eutectic HEAs, highlighting its great potential as advanced structural materials.

Additionally, the fracture surfaces were examined using SEM, as shown in Fig. 7. The overall fracture morphologies reveal that the CR760 alloy undergoes uniform deformation without necking (Fig. 7a). In contrast, pronounced necking is observed in the CR800 alloy after tensile testing (Fig. 7d). Furthermore, the fracture surfaces of both alloys exhibit two distinct regions: the peripheral shear lip zone and the central flat fracture zone. Enlarged SEM images reveal that the central flat fracture zones of both alloys exhibit a micro-void coalescence fracture mode with numerous dimples. In the peripheral shear lip region, the dimples are notably finer compared to those observed in the central region. Thus, both alloys exemplify typical characteristics of ductile fracture.

3.4. The evolution of back stress and effective stress

To identify the origin of the differences in strain hardening behaviour between CR760 and CR800 alloys, LUR tests were conducted to characterize the evolution of flow stress distribution in these two alloys, as shown in Fig. 8a. Magnified LUR curves in Fig. 8b show distinct hysteresis loops of both CR760 and CR800 samples, which are indicative of the Bauschinger effect [44]. The macroscopic flow stress in heterogeneous-structured materials can be divided into back stress and effective stress, depending on the range of stress induced by dislocation interactions with various obstacles [45]. Specifically, back stress is a long-range stress arising from geometric necessary dislocations accumulated at the boundaries of heterogeneous structures, grains, dislocation walls, and non-coherent precipitates [36,46]. Effective stress, on the other hand, is a short-range stress that addresses obstacles over short distances, such as solute atoms, short-range ordering, and forest dislocations [36,47].

The back and effective stresses for both alloys were calculated using the method proposed by Yang et al. [46], with their variation as a function of true strain shown in Fig. 8c and d. In the early stages of deformation (true strain below 8 %), back stress in both CR760 and CR800 alloys increased, while effective stress decreased with continued deformation. As deformation progressed, the CR800 alloy exhibited

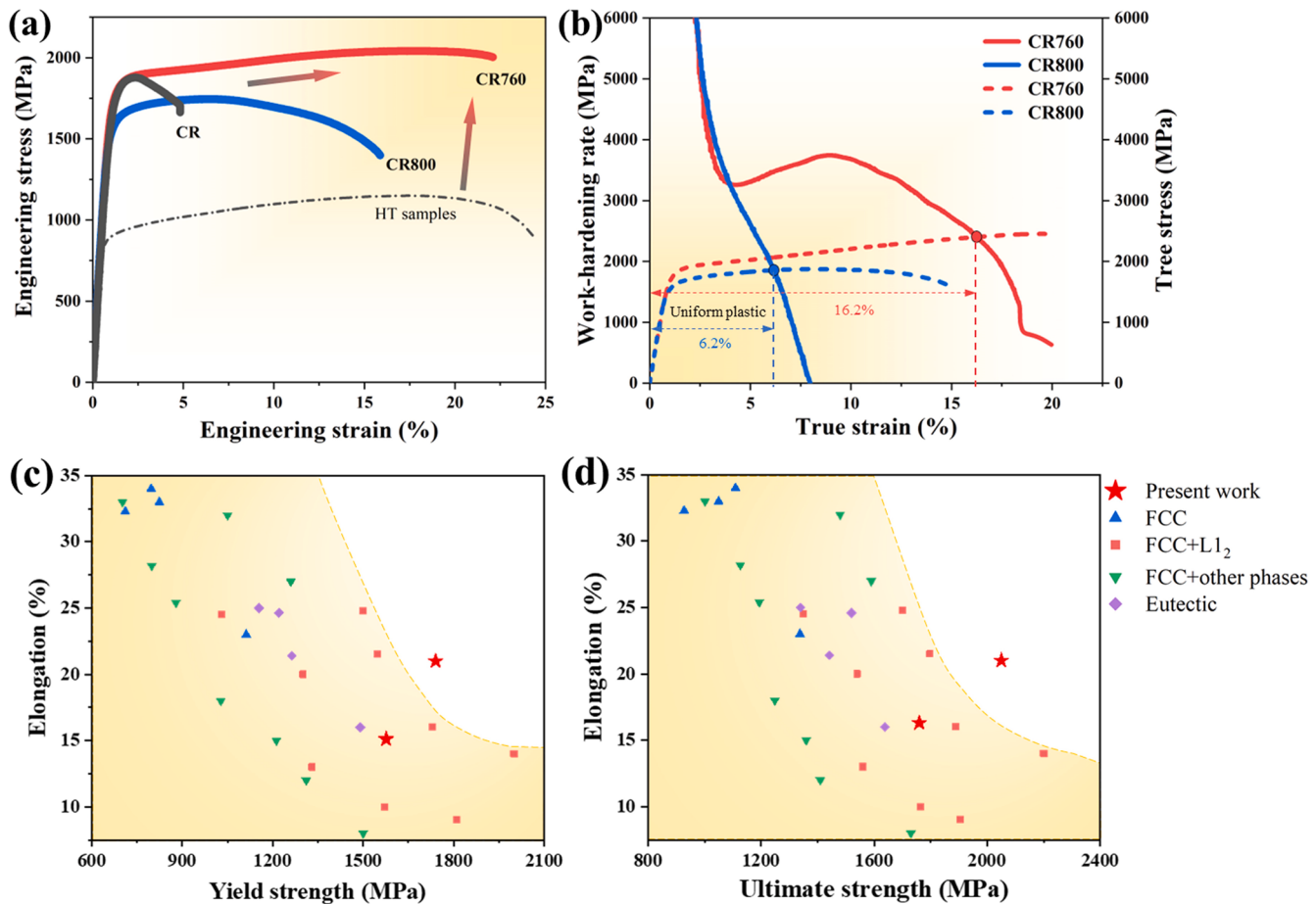


Fig. 6. Mechanical responses of the $\text{Al}_5\text{Ti}_8(\text{FeCoNi})_{86.9}\text{B}_{0.1}$ HEA after different processes. (a) Tensile curves of the HT, CR, CR760, and CR800 alloys. (b) Work-hardening behaviours of the CR760 and CR800 alloys. Comparison of mechanical properties between the HEAs in this study and other heterogeneous-structured HEAs with single FCC phase [17,33,34], FCC+L1₂ phases [30,35–38], FCC+other phases [39–41], or eutectic microstructure [42,43]: (c) Yield strength versus elongation. (d) Ultimate strength versus elongation.

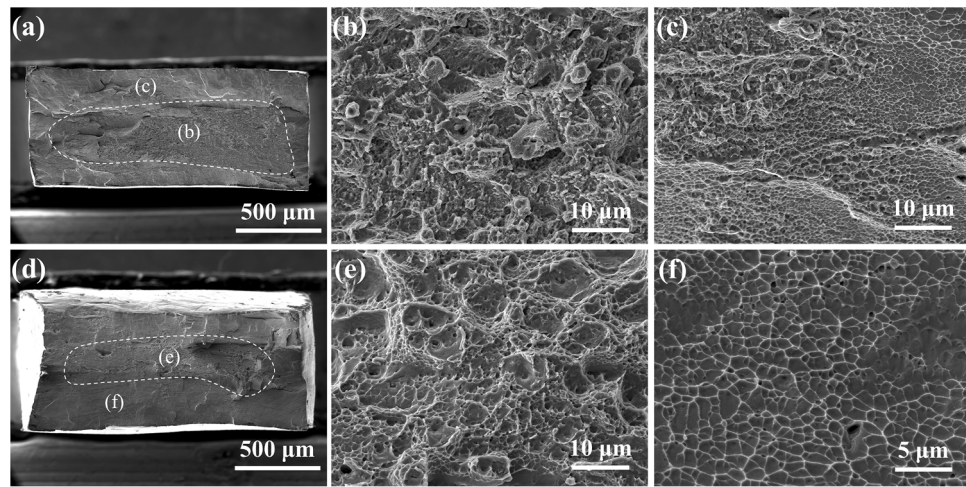


Fig. 7. Fracture morphologies of the CR760 and CR800 alloys. (a-c) CR760. (d-f) CR800. (a, d) Overview of the fracture surface. (b, e) High magnification of the central fracture region. (c, f) High magnification of the peripheral shear lip region.

insufficient strain-hardening capacity, resulting in necking and eventual fracture. In contrast, the back stress of the CR760 alloy remained stable approximately 1300 MPa, and the effective stress increases, contributing to enhanced flow stress at later stages. This demonstrates that the increased effective stress in the CR760 alloy is the primary source of

strain hardening, suggesting the emergence of an additional factor contributing to the effective stress in the later stages compared to the CR800 alloy.

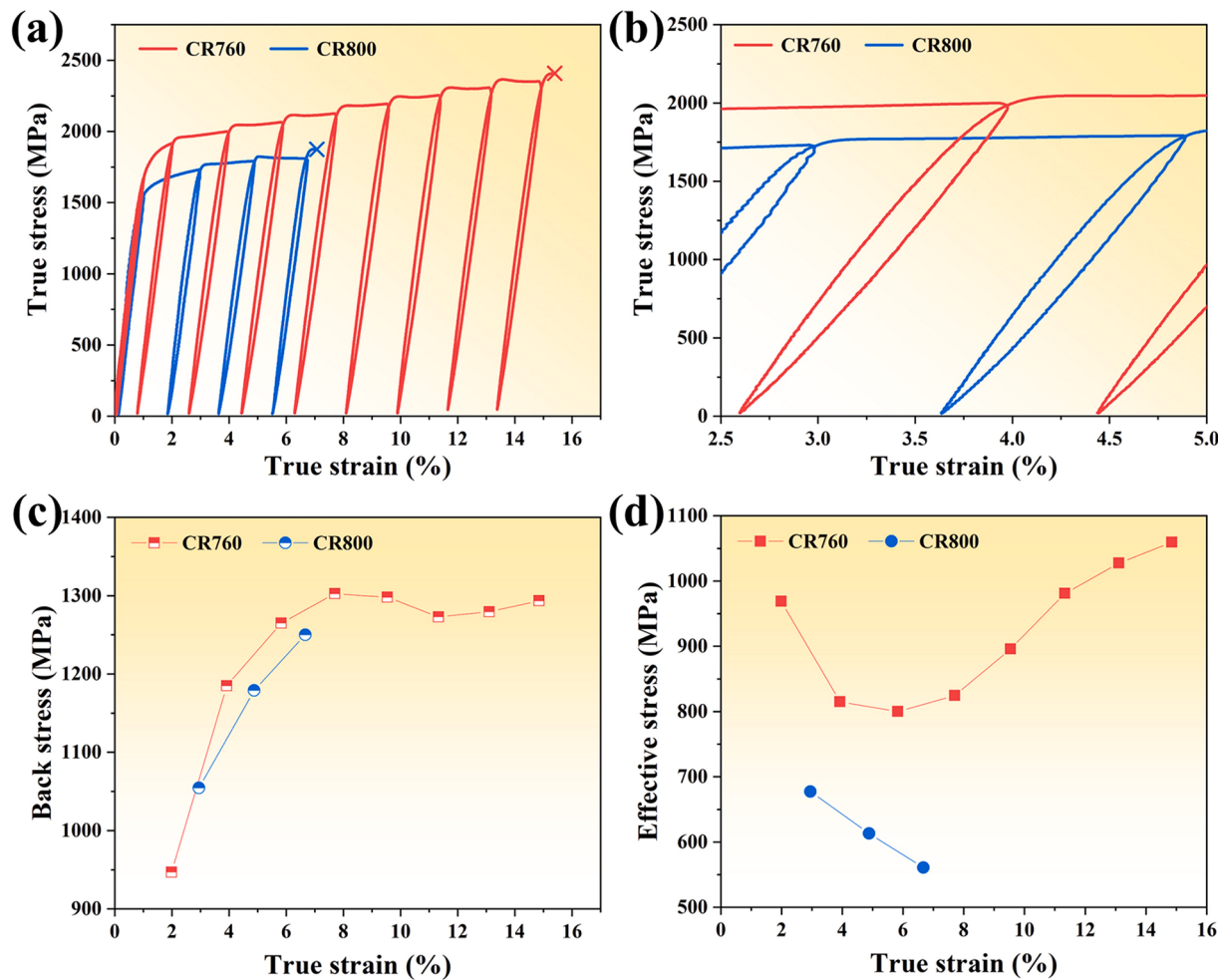


Fig. 8. Flow stress partitioning behaviour of the CR760 and CR800 alloys. (a) True stress-strain curves of LUR test. (b) An enlarged view of the hysteresis loop taken from (a). (c) Evolution of back stress with the variation of true strain. (d) Evolution of effective stress with the variation of true strain.

4. Discussion

In this study, both the CR760 and CR800 alloys with heterogeneous microstructures exhibit ultrahigh strength and excellent ductility. Specifically, the CR760 alloy possesses an elongation of 21.0 % and an ultimate strength of 2.05 GPa due to its sustained and elevated strain hardening. To correlate the mechanical behaviour with the heterogeneous microstructure containing L1₂ precipitates, the strengthening and strain hardening mechanisms were systematically investigated and discussed.

4.1. Strengthening mechanism

As indicated in Sections 3.1 and 3.2, the CR760 and CR800 alloys are primarily composed of NRX regions, as well as a small fraction of RX areas. For simplicity in calculating strengthening mechanisms, the recrystallized regions are approximated as FCC grains despite containing a minor BCC phase, and it is also assumed that these recrystallized grains contain L1₂ phase with a volume fraction equal to that of the NRX regions. Consequently, the yield strength (σ_y) is typically the sum of the contributions from various strengthening mechanisms, which can be expressed as Eq. (1):

$$\sigma_y = \sigma_0 + \sigma_s + \sigma_d + \sigma_p + \sigma_g f_{RX} \quad (1)$$

where σ_0 and σ_s represent the lattice friction stress and solid solution strengthening, respectively. Since the conventional solute strengthening

models for dilute solid solutions are not suitable for HEAs with multi-principal elements [48], this study estimates the sum of σ_0 and σ_s as 277 MPa, referencing Fe_{42.26}Ni_{27.5}Co_{17.5}Al_{10.5}Ta_{2.2}B_{0.04} HEA [49]. σ_d , σ_p , and σ_g represent the contributions from dislocation strengthening, L1₂ precipitates strengthening and grain boundary strengthening, respectively, while f_{RX} corresponds to the volume fraction of the RX region. The general mixture rule was applied to evaluate the contribution of grain boundary strengthening in the recrystallized regions to the overall yield strength of the alloys based on their microstructural characteristics.

The high dislocations density in the alloy contributes to dislocation strengthening, which can be calculated by Eq. (2) [50]:

$$\sigma_d = M\alpha Gb\sqrt{\rho} \quad (2)$$

where $M = 3.06$ is the Taylor factor and α is a constant for FCC alloys, typically taken as 0.2 [51]. The Burgers vector, $b = \sqrt{2}a/2$, determined by XRD analysis, is 0.243 nm for the CR760 alloy and 0.244 nm for the CR800 alloy. The shear modulus $G = 78.5$ GPa is taken from the (FeCoNiCr)₉₄Ti₂Al₄ alloy [15]. The dislocation density (ρ) is generally the sum of the geometrically necessary dislocations (GNDs) density (ρ_{GND}) and the statistically stored dislocations (SSDs) density (ρ_{SSD}) in the alloy. Previous studies have shown that ρ_{SSD} typically constitutes about 15–35 % of the total dislocation density under annealing conditions [50,52]. Given that the alloys were annealed at 760 and 800 °C for two hours, it is assumed that ρ_{SSD} constitutes 20 % of the total dislocation density in this study [51]. The densities of GNDs are estimated from

the EBSD results in Fig. 2, with values of approximately $22.0 \times 10^{14} \text{ m}^{-2}$ for the CR760 alloy and $14.1 \times 10^{14} \text{ m}^{-2}$ for the CR800 alloy. Based on the measured ρ_{GND} , the final dislocation densities in the CR760 and CR800 alloys are 27.5×10^{14} and $17.6 \times 10^{14} \text{ m}^{-2}$, respectively. Consequently, the contributions of dislocation strengthening to the yield strength are calculated to be 612 MPa for the CR760 alloy and 492 MPa for the CR800 alloy.

For nanosized coherent L₁₂ precipitates, the typical precipitation strengthening mechanism is the dislocation shearing mechanism, which is commonly observed in L₁₂-strengthened HEAs [53,54]. The precipitation strengthening mechanism is described by Eq. (3) [55]:

$$\sigma_p = 0.81M\left(\gamma_{apb}/2b\right)(3\pi f/8)^{1/2} \quad (3)$$

where γ_{apb} represents the antiphase boundary energy of the L₁₂ phase, with a value of 0.2 J/m^2 obtained from the Ni₃(Al, Ti) phase in Ni-based superalloys [56], and f is the volume fraction of the L₁₂ phase. Accordingly, the strengthening contributions of L₁₂ phase to the yield strength are 751 MPa for the CR760 alloy and 740 MPa for the CR800 alloy.

Grain boundary strengthening is commonly described by the Hall-Petch relationship [57], as illustrated in Eq. (4):

$$\sigma_d = k_y d^{-1/2} \quad (4)$$

where k_y is the Hall-Petch coefficient, taken as $440 \text{ MPa}\cdot\mu\text{m}^{1/2}$ from the Fe_{42.26}Ni_{27.5}Co_{17.5}Al_{10.5}Ta_{2.2}B_{0.04} HEA [49]. The parameter d represents the average grain size in the RX region. Therefore, the grain boundary strengthening contributions are determined as 80 MPa for the CR760 alloy and 92 MPa for the CR800 alloy.

Fig. 9 presents a clear comparison between the sum of the calculated contributions from various strengthening mechanisms and the measured yield strength. The results indicate a good agreement between the predicted values and the experimental data. Furthermore, the notably high yield strength of the alloys is predominantly attributed to effective dislocation strengthening and L₁₂ precipitates strengthening. The yield strength difference between CR760 and CR800 alloys is mainly attributed to dislocation strengthening, with the higher dislocation recovery in CR800 reducing its strengthening effect.

4.2. Deformation behaviour

To correlate the work-hardening behaviour with the underlying deformation mechanisms, the microstructural evolution of the CR760 alloy after deformation was investigated using μ -DIC, TEM, and XRD.

4.2.1. Enhanced ductility through deformation of NRX regions

Reported alloys with heterogeneous microstructure typically consist of a mix of coarse and fine grains [38,39], or a combination of fine recrystallized grains, ultrafine grains, and non-recrystallized regions [17,58]. These heterogeneous microstructures, resulting from partial recrystallization or uneven grain growth, often exhibit non-uniform strain behaviour between different regions [19]. In the CR760 and CR800 alloys, limited recrystallization led to the formation of ultrafine grains, while the majority of regions remained non-recrystallized. Additionally, a significant number of nano-scaled L₁₂ phases uniformly precipitated within the RX and NRX regions. The deformation behaviour within this multi-scale, multi-phase heterogeneous microstructure is expected to differ significantly from that of existing alloys. Based on this, the CR760 alloy was chosen for quantitative analysis of its heterogeneous deformation behaviour using μ -DIC.

Fig. 10 presents an approximately $8 \times 8 \mu\text{m}^2$ region containing both PRX and NRX areas (Fig. 10a), demonstrating the microscopic strain distribution during macroscopic tensile deformation. At a global strain of 1.1 % (Fig. 10b), the strain distribution appears relatively uniform in the PRX area with minor, weak strain accumulation points. In contrast, pronounced strain accumulation bands are evident in the NRX region. As the strain increases to 3.4 % (Fig. 10c), both the PRX and NRX regions display significant strain behaviour. The reddening of the deformation bands in the NRX regions indicates an increased distribution of strain within them. Additionally, the strain distribution within the PRX region is uneven, likely due to the mechanical property differences between the RX and NRX grains. Figs. 10d and e illustrate the strain distribution in the alloy at global strain levels of 9.4 % and 17.5 %, respectively, using an alternative scale for clarity. At elevated strain levels, the RX in the PRX regions starts to accommodate more strain, with strain distribution behaviour becoming increasingly prominent. Fig. 10f presents an enlarged view of Fig. 10e overlapped with the original microstructure, revealing that the areas with intense deformation are predominantly located within the RX regions, some of which are highlighted in the red-marked regions in Fig. 10a. Therefore, the heterogeneous strain

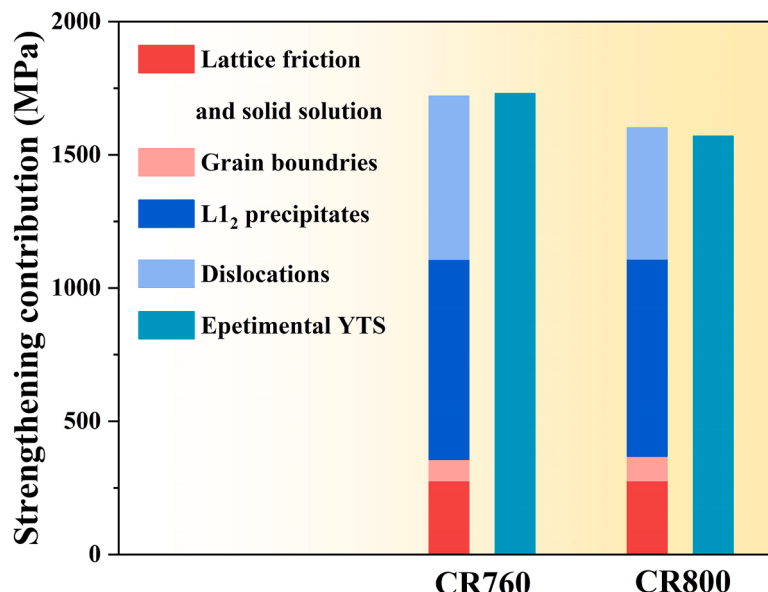


Fig. 9. Calculated strengthening mechanisms and experimental YTS of CR760 and CR800 alloys.

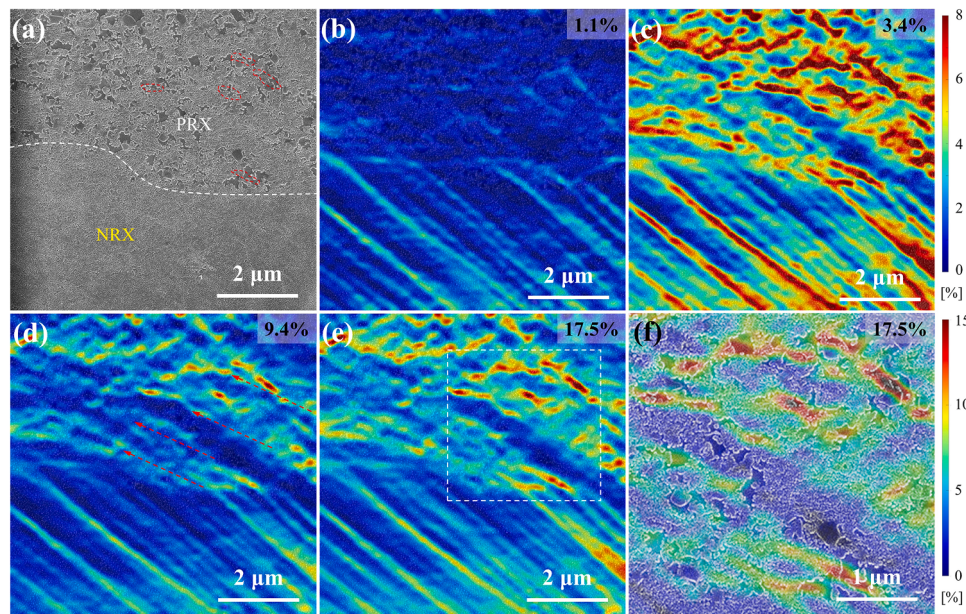


Fig. 10. Micro-strain distribution in PRX and NRX regions of the CR760 alloy under different global strains analyzed using μ -DIC. (a) The initial microstructure includes PRX and NRX regions. Strain distribution maps at different strain levels: (b) 1.1 %, (c) 3.4 %, (d) 9.4 %, (e) 17.5 %. (f) The enlarged region in (e) overlapped with the original microstructure figure.

behaviour and evolution within the PRX and NRX regions serve as sources of long-range back stress, significantly contributing to its increase with strain, as shown in Fig. 8c. Additionally, the heterogeneous deformation in the PRX and NRX regions appears to be interdependent, with the deformation in the PRX regions extending from the strain bands in the NRX areas, as indicated by the red arrows in Fig. 10d. Similar phenomena were also observed in another region. This continuous strain behaviour mitigates stress concentration at the interfaces between PRX and NRX, promoting uniform deformation throughout the alloy.

Notably, existing research indicates that the recrystallized regions in heterogeneous-structured alloys predominantly bear the deformation, either approaching or exceeding the average macroscopic strain, thereby maintaining deformation compatibility [30,31,34]. For instance, during the deformation of the heterogeneous-structured Ni₂CoCrFeTi_{0.24}Al_{0.2} HEA, large grain regions experience the highest strain, followed by small grain regions, while NRX regions remain largely undeformed [30]. In another heterogeneous-structured CoCrNi alloy, the local strain in the RX regions is an order of magnitude higher than that in the NRX regions after deformation [34]. This strain distribution correlates with the properties of various regions, where lower-strength areas tend to yield first and subsequently accommodate more significant plastic deformation. In this study, it is observed that during the deformation of CR760 alloy, the NRX regions primarily undergo deformation through the reactivation and coarsening of pre-existing deformation bands. Furthermore, due to the significantly higher volume fraction of NRX regions, these areas accommodate the majority of the deformation, contributing to the excellent ductility of both CR760 and CR800 alloys, a phenomenon not commonly observed in existing heterogeneous-structured alloys.

This phenomenon of early deformation in the NRX regions suggests that dislocation nucleation and slip are more favourably activated in these areas during the initial stages of deformation than in the RX regions. Two primary factors contribute to the pronounced dislocation activities in the NRX region. Firstly, the NRX regions have a lower critical stress for yielding compared with that of the RX regions. As detailed in Section 4.1, the variation in yield strength between the NRX and RX regions is primarily due to the disparity between dislocation strengthening and grain boundary strengthening (without considering

the dislocation strengthening in the RX regions). For CR760 alloy, nanoscaled recrystallized grains provide 1100 MPa to the yield strength of the RX regions through Hall-Petch strengthening, while dislocation strengthening accounts for 620 MPa (calculated using Eq. (2) and $\rho_{GND}=28.2 \times 10^{14} m^{-2}$ of NRX region) of the NRX regions. This difference results in a lower critical yield strength of the NRX regions. Moreover, the dislocation density in the NRX regions is markedly higher than that in the RX regions. The significantly high dislocation density provides numerous nucleation sites for dislocation multiplication [17, 59, 60]. Under these two conditions, plastic deformation is more likely to initiate in the NRX regions.

4.2.2. Deformation mechanism of CR760 alloy

The deformation microstructure of the CR760 alloy after tensile testing was further characterized using TEM, as illustrated in Fig. 11. In the NRX region, tensile deformation not only thickened the existing deformation bands by dislocation accumulation but also activated new ones in multiple directions, as shown in Fig. 11a. Fig. 11b presents the deformed recrystallized microstructure, where high-density dislocation tangles within the FCC grains indicate that these grains have undergone severe plastic deformation. Few dislocation features are observed inside the BCC grains (Fig. 11c). In contrast, distinct dislocation pile-ups are noted at their boundaries. This phenomenon indicates that the BCC phase strengthens the alloy by hindering dislocation motion and generating long-range back stress during deformation.

Fig. 11d shows an enlarged BF-TEM image of the NRX region, revealing numerous dark spheroidal structures with extensive strain-induced stripes. DF-TEM and the corresponding SAED pattern in Fig. 11e confirm that these dark spheroidal structures are L1₂ precipitates. The elongated superlattice diffraction spots in the SAED pattern (Fig. 11f) indicate orientation differences within the L1₂ phase. Fig. 11g illustrates that strain-induced stripes are found in both the FCC matrix and the L1₂ phase, with a notable concentration at their interface. Additionally, geometric phase analysis (GPA) was conducted to compare the atomic strain fluctuations within both the L1₂ phase and the matrix before and after tensile testing (Figs. 11h and i). Fig. 11h illustrates the relatively minor localized lattice distortions in both the FCC matrix and the L1₂ phase. In contrast, after deformation, Fig. 11i shows significantly larger atomic strain fields in both phases. These findings indicate that

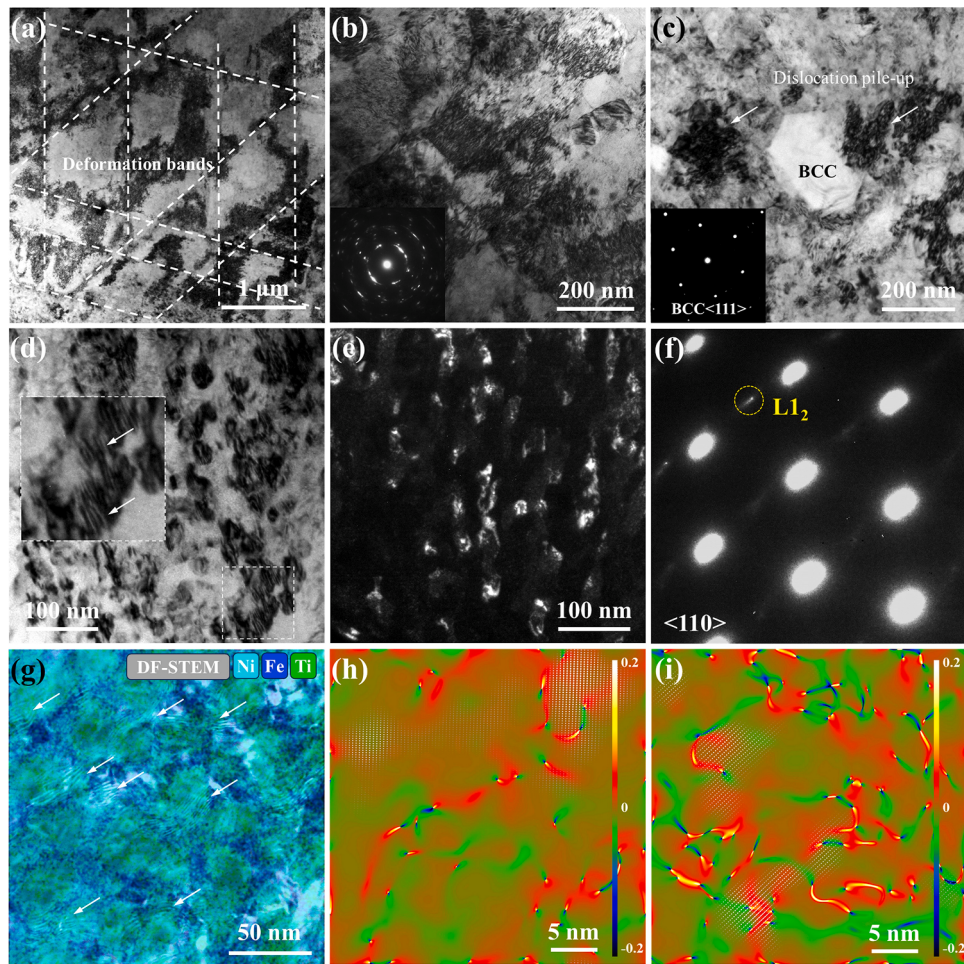


Fig. 11. Deformation microstructure of the CR760 alloy characterized by TEM. (a) BF-TEM of deformation bands in NRX region. (b) BF-TEM image of FCC grains in RX region, with the inset showing the corresponding SAED pattern. (c) BF-TEM image of the BCC grain in the RX region, with the inset showing the corresponding SAED pattern. (d) and (e) are BF-TEM and DF-TEM of the L₁₂ particles, respectively. (f) Corresponding SAED pattern of (e). (g) Overlay of dark field STEM and EDS maps illustrating the distributions of the L₁₂ phase (indicated by the distribution of Ni, Fe, and Ti elements) and the strain-induced stripes. The GPA strain maps (ϵ_{xy}) before (h) and after (i) tensile testing, overlaid with an inverse fast Fourier transform (IFFT) image of L₁₂ phase superlattice diffraction spots by a Bragg filter, illustrating stress concentration in both FCC and L₁₂ phases in the alloys.

the numerous L₁₂ precipitates in the NRX regions have undergone significant deformation in synergy with the FCC matrix. Two factors contribute to this phenomenon: First, the coherent interface between the L₁₂ precipitates and the FCC matrix allows dislocations to pass through, reducing stress concentration and promoting uniform plasticity. Second, the multi-component L₁₂ phase in HEAs has been proven to exhibit exceptional plastic deformation capabilities and greatly enhance the tensile ductility of the L₁₂-strengthened HEAs [61,62]. Together, these characteristics are critical for the NRX regions to accommodate the majority of the deformation.

4.2.3. Origins of superior strain hardening of CR760 alloy

It is well-known that ultra-strong alloys with high-density dislocations usually exhibit limited strain-hardening ability due to the saturation of dislocation multiplication [63]. In contrast, the CR760 alloy demonstrates a significantly higher strain-hardening rate, resulting in superior uniform elongation and tensile strength. Although strain hardening can be improved through mechanisms like deformation twinning [64] and microbands [65], these structures were not present in the studied alloys.

To understand the cause of the excellent strain hardening observed in the CR760 alloy, we conducted XRD characterization on the fractured CR760 (CR760-F) and CR800 (CR800-F) samples, as depicted in Figs. 12a-c. It is evident that the BCC (110) peak near 52° of the CR760-F

sample is significantly intensified compared to the pre-deformed sample (Fig. 12b). Additionally, a BCC (211) diffraction peak emerges near 99°, which was absent in the pre-deformed sample (Fig. 12c). Furthermore, HR-TEM (Fig. 12d) and corresponding FFT patterns (Fig. 12e) revealed an atomic-scale FCC→BCC phase transformation in the NRX region. The FCC phase and the deformation-induced BCC phase exhibit a semi-coherent relationship, characterized by $(\bar{1}\bar{1}1)_{\text{FCC}}//(\bar{1}\bar{1}0)_{\text{BCC}}$ and $[011]_{\text{FCC}}//[\bar{1}\bar{1}1]_{\text{BCC}}$ orientation relationships, typical characteristic of the Kurdjumov-Sachs (K-S) orientation relationship, as illustrated in Fig. 12e. Fig. 12f presents the corresponding IFFT image, highlighting short-range BCC phase domains produced by FCC→BCC phase transformation. Consequently, the XRD and TEM analyses reveal the formation of numerous dispersed, short-range and semi-coherent BCC domains during the deformation of the CR760 alloy. The FCC→BCC transformation effect not only promotes plastic deformation by aligning the crystal structure for more efficient dislocation movement but also introduces phase boundaries that impede dislocation motion, thus significantly enhancing ductility and strain-hardening capability [13, 66]. Notably, the semi-coherent BCC domains will lead to short-range interactions with dislocations, which explains the increase in the effective stress of CR760 alloy observed in Fig. 8d [19]. Therefore, it can be concluded that the phase transformation-induced plasticity effect maintains a high level of strain hardening and improves the flow stress

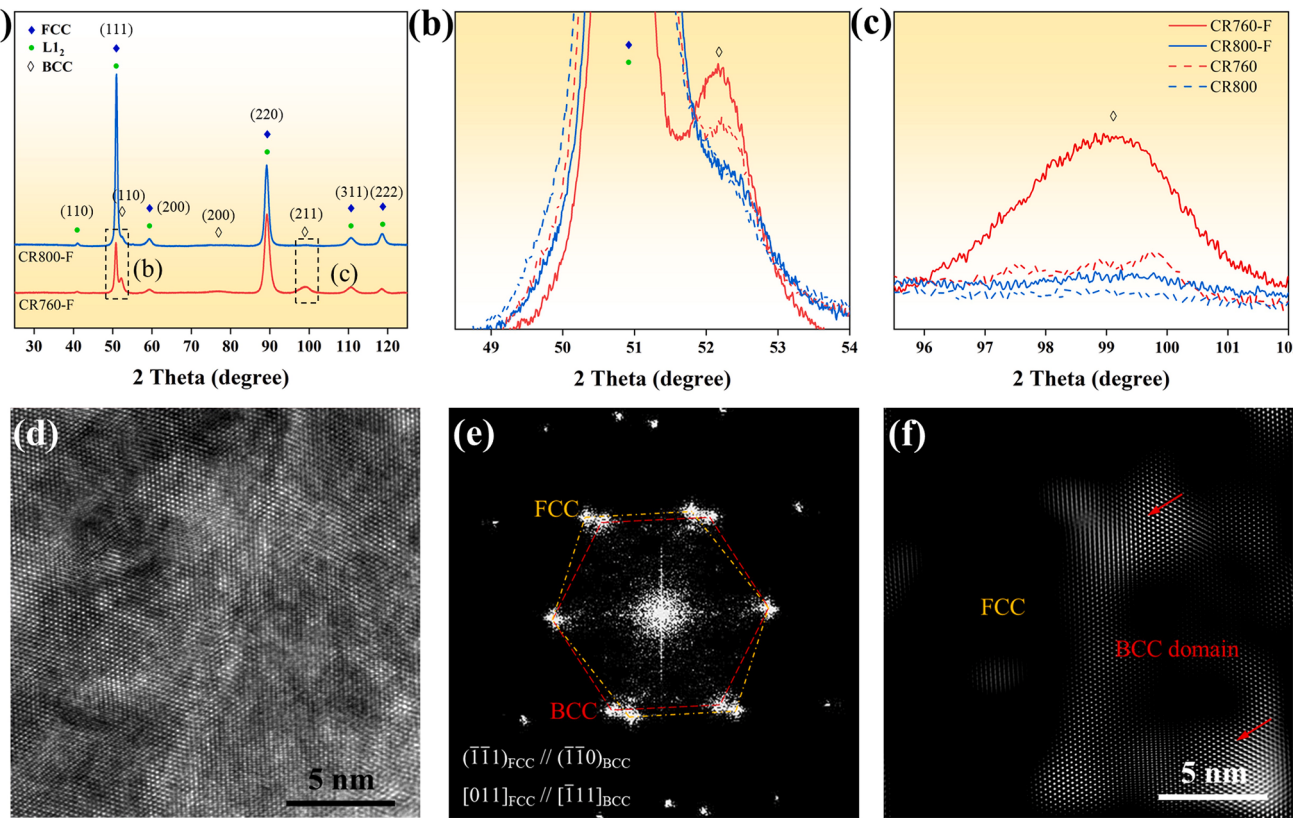


Fig. 12. Characterization of phase transformation in CR760 and CR800 alloys after tensile testing. XRD analysis: (a) XRD patterns for CR760-F and CR800-F samples. (b) Magnified views of the BCC (110) diffraction peak. (c) Magnified views of the BCC (211) diffraction peak. Atomic-scale evidence of FCC→BCC phase transformation in NRX regions: (d) HR-TEM image. (e) Corresponding FFT showing the orientation relationship between FCC and BCC phases. (f) Corresponding IFFT image of BCC domains obtained using a Bragg filter.

in the later stages of deformation by elevating effective stress. In comparison, the XRD pattern of the CR800-F sample shows negligible FCC→BCC phase transformation during deformation, explaining its lower flow stress and strain hardening capacity. This further confirms that the superior work-hardening ability of the CR760 alloy originates from the FCC→BCC phase transformation [67,68].

However, why does the CR800 alloy, despite having the same composition and a similar microstructure, not undergo phase transformation? Two main factors can explain this. Initially, the CR760 alloy exhibits a higher phase transformation driving force. The Gibbs free energies for the formation of FCC and BCC phases were calculated based on the FCC matrix compositions of both alloys using JMatPro software. Although the Gibbs free energy calculations derived from the phase diagram are approximate, they effectively illustrate the general trend and offer valuable insights into the thermodynamic driving forces governing diffusion-less phase transformations [68]. Calculations show that the Gibbs free energy difference ($\Delta G = 1184 \text{ J/mol}$) between the FCC ($-16,662 \text{ J/mol}$) and BCC ($-17,846 \text{ J/mol}$) phases in the CR760 alloy is more significant than that ($\Delta G = 619 \text{ J/mol}$) in the CR800 alloy, suggesting a stronger thermodynamic driving force for the phase transformation in the CR760 alloy. Additionally, under the same amount of deformation, the CR760 alloy exhibits greater dislocation density, resulting in a significantly higher flow stress than the CR800 alloy. The mechanical driving force generated from the applied stress might compensate for the chemical driving force, further facilitating phase transformation in the CR760 alloy [69,70]. Consequently, the more unstable matrix and higher stress in the CR760 alloy promote FCC→BCC phase transformation, thereby enhancing its strain-hardening capability. Notably, based on the above analysis, the L1₂ phase precipitation offers a dual benefit to the alloy: it not only significantly improves the mechanical strength but also induces the formation of a metastable FCC

matrix, which actively drives phase transformation during deformation, thereby enhancing strain hardening [68,71].

4.3. Exceptional mechanical properties associated with microstructure evolution

In this study, the impressive strength-ductility combination of the CR760 alloy significantly surpasses that of other reported heterogeneous-structured HEAs (Fig. 6). This performance enhancement is attributed to the synergy of multiple strengthening mechanisms achieved through microstructural manipulation.

Fig. 13 provides a schematic summary of the microstructural evolution following thermomechanical processing and tensile deformation. As previously mentioned, the original HT alloy consists of coarse FCC grains (Fig. 2a). Cold rolling induces significant deformation in the alloy, resulting in the formation of shear bands cutting through multiple grains and deformation bands within the grains (Fig. 2b and Fig. 13a). The substantial dislocation pile-up significantly increases the yield strength of the CR alloy. Following annealing at 760 and 800 °C, a limited number of ultrafine grains are formed within the shear bands, accompanied by nano-scale L1₂ precipitates inside the grains and some BCC grains around them. Both RX and NRX areas in the shear bands contribute to the formation of PRX regions (Fig. 2d₁, e₁ and Fig. 13b). In the NRX regions, a significant number of coherent L1₂ phases are uniformly precipitated. This microstructure effectively harnesses the synergistic effects of dislocation strengthening, L1₂ precipitates strengthening and grain boundary strengthening, leading to a yield strength comparable to that of the CR sample. Such excellent yield strength following annealing is seldom observed in existing heterogeneous-structured HEAs. Moreover, the combination of L1₂ precipitates strengthening and grain boundary strengthening leads to

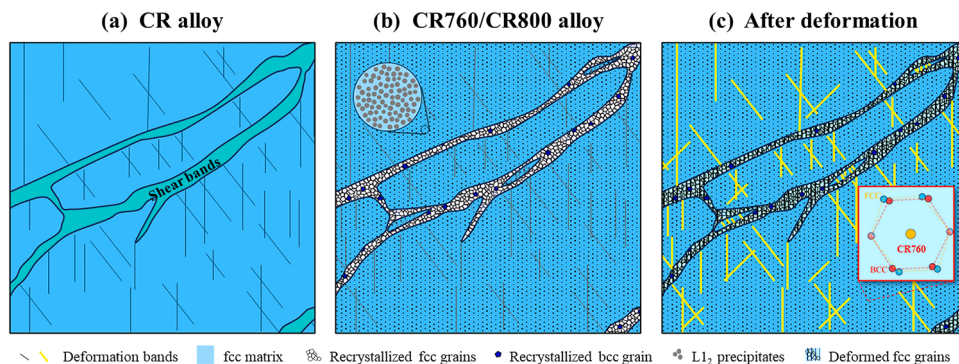


Fig. 13. Schematic sketches illustrating the microstructure evolution of the experimented samples.

higher yield strength of the RX regions compared to the NRX areas. This results in preferential deformation of the NRX regions, which primarily accommodate the tensile strain through the proliferation of dislocations within the shear bands and the synergistic deformation of the L₁₂ and the FCC phases (Fig. 13c). Importantly, following annealing, a metastable FCC phase forms around the L₁₂ precipitates, promoting the phase transformation from FCC to BCC during deformation. This transformation enhances strain hardening, allowing the alloy to sustain excellent elongation and ultimate strength, even at high yield strength. Deformation and strain hardening in the NRX regions are relatively rare, as these areas are generally considered to contribute mainly to the strengthening of the alloy without undergoing deformation or strain hardening. Nonetheless, in this study, they serve as the primary deformation mechanisms, significantly enhancing the tensile ductility and strength of the CR760 alloy.

5. Conclusions

In this study, the heterogeneous-structured Al₅Ti₈(FeCoNi)_{86.9}B_{0.1} HEA achieved an exceptional combination of strength and ductility through the deformation and strain hardening of non-recrystallized regions. The key conclusions drawn from the experimental results and analysis are as follows:

1. The heterogeneous microstructure, composed of large non-recrystallized regions and small fractions of ultrafine recrystallized grains, was produced through cold-rolling and annealing in the FCC + L₁₂ two-phase region. A high density of L₁₂ phases precipitated throughout both recrystallized and non-recrystallized areas. As the annealing temperature rose from 760 to 800 °C, both the grain size and volume fraction of the recrystallized grains increased.
2. The alloy annealed at 760 °C achieved a yield strength of 1.73 GPa, an ultimate strength of 2.05 GPa, and an elongation of 21.0 %, which significantly outperformed the counterpart alloy annealed at 800 °C and other reported heterogeneous-structured HEAs.
3. The high yield strength of the heterogeneous-structured alloy mainly results from dislocation strengthening, L₁₂ precipitates strengthening, and grain boundary strengthening. During subsequent deformation, the non-recrystallized regions absorbed significant strain through the reactivation of deformation bands and the synergistic deformation of FCC and L₁₂ phases.
4. For the alloy annealed at 760 °C, the metastable FCC matrix, driven by significant phase transformation force and high stress, facilitated the atomic-scale FCC→BCC phase transformation. This led to the formation of numerous short-range BCC domains, which further enhanced strain hardening.

Overall, this innovative strategy, which involves deformation and strain hardening in non-recrystallized regions, offers a promising approach for developing alloys with exceptional strength and ductility.

It could also be applied to other traditional metallic systems to achieve superior performance in targeted applications.

CRediT authorship contribution statement

Hongchao Li: Writing – original draft, Methodology, Investigation, Formal analysis, Data curation, Conceptualization. **Jun Wang:** Writing – review & editing, Validation, Resources, Funding acquisition, Conceptualization. **Wenyuan Zhang:** Software, Methodology. **Jiawang Zhao:** Methodology, Investigation, Data curation. **Jinshan Li:** Writing – review & editing, Resources, Funding acquisition. **M.W. Fu:** Writing – review & editing, Validation, Supervision, Resources.

Declaration of competing interest

We declare that we have no financial and personal relationships with other people or organizations that can inappropriately influence our work. There is no professional or other personal interest of any nature or kind in any product, service or company that could be construed as influencing the position presented in or the review of the manuscript entitled. The work described has not been submitted elsewhere for publication, in whole or in part, and all the authors listed have approved the manuscript that is enclosed.

Acknowledgements

This work was supported by the National Key Research and Development Program (2022YFB3707103), the Natural Science Foundation of China (52174375), the Key Research and Development Program of Shaanxi (2022JBGS2–04), the fund of the State Key Laboratory of Solidification Processing in NWPU (2023-TS-13), and the projects of 1-ZE1W and 4-WZ4W funded by the Hong Kong Polytechnic University.

References

- [1] M.A. Meyers, A. Mishra, D.J. Benson, Mechanical properties of nanocrystalline materials, *Prog. Mater Sci.* 51 (2006) 427–556.
- [2] E. Ma, X. Wu, Tailoring heterogeneities in high-entropy alloys to promote strength-ductility synergy, *Nat. Commun.* 10 (2019) 5623.
- [3] Z. Li, S. Ma, S. Zhao, W. Zhang, F. Peng, Q. Li, T. Yang, C.-Y. Wu, D. Wei, Y.-C. Chou, P.K. Liaw, Y. Gao, Z. Wu, Achieving superb strength in single-phase FCC alloys via maximizing volume misfit, *Mater. Today* 63 (2023) 108–119.
- [4] M. Niu, G. Zhou, W. Wang, M.B. Shahzad, Y. Shan, K. Yang, Precipitate evolution and strengthening behavior during aging process in a 2.5 GPa grade maraging steel, *Acta Mater.* 179 (2019) 296–307.
- [5] S. Wang, W. Wu, Y. Sun, Z. Yang, G. Sha, W. Wang, Z. Jiao, H. Chen, Regulating precipitation behavior in an ultrahigh-strength, high-molybdenum maraging steel via laser powder bed fusion, *Scr. Mater.* 252 (2024) 116245.
- [6] J.R. Weertman, 12 Mechanical Behavior of Nanocrystalline Metals, in: C.C. Koch (Ed.), *Nanostructured Materials*, William Andrew Publishing, NY, 2007, pp. 537–564.
- [7] C.C. Koch, D.G. Morris, K. Lu, A. Inoue, Ductility of nanostructured materials, *MRS Bull.* 24 (1999) 54–58.

- [8] V. Yamakov, D. Wolf, S.R. Phillpot, A.K. Mukherjee, H. Gleiter, Dislocation processes in the deformation of nanocrystalline aluminium by molecular-dynamics simulation, *Nat. Mater.* 1 (2002) 45–49.
- [9] S. Zhang, R. Li, H. Kang, Z. Chen, W. Wang, C. Zou, T. Li, T. Wang, A high strength and high electrical conductivity Cu-Cr-Zr alloy fabricated by cryorolling and intermediate aging treatment, *Mater. Sci. Eng. A* 680 (2017) 108–114.
- [10] D. Wei, W. Gong, L. Wang, B. Tang, T. Kawasaki, S. Harjo, H. Kato, Strengthening of high-entropy alloys via modulation of cryo-pre-straining-induced defects, *J. Mater. Sci. Technol.* 129 (2022) 251–260.
- [11] C. Herrera, D. Ponge, D. Raabe, Design of a novel Mn-based 1 GPa duplex stainless TRIP steel with 60% ductility by a reduction of austenite stability, *Acta Mater.* 59 (2011) 4653–4664.
- [12] W. Mao, S. Gao, W. Gong, Y. Bai, S. Harjo, M.-H. Park, A. Shibata, N. Tsuji, Quantitatively evaluating respective contribution of austenite and deformation-induced martensite to flow stress, plastic strain, and strain hardening rate in tensile deformed TRIP steel, *Acta Mater.* 256 (2023) 119139.
- [13] Z. Li, K.G. Pradeep, Y. Deng, D. Raabe, C.C. Tasan, Metastable high-entropy dual-phase alloys overcome the strength-ductility trade-off, *Nature* 534 (2016) 227–230.
- [14] W. Lu, J. Gong, B. Huang, Y. Wang, X.-S. Yang, X. Luo, R. Hu, Y. Yang, Optimizing precipitation hardening in a L₁₂-strengthened medium-entropy alloy via tuning the anti-phase boundary energy, *Scr. Mater.* 245 (2024) 116045.
- [15] J.Y. He, H. Wang, H.L. Huang, X.D. Xu, M.W. Chen, Y. Wu, X.J. Liu, T.G. Nieh, K. An, Z.P. Lu, A precipitation-hardened high-entropy alloy with outstanding tensile properties, *Acta Mater.* 102 (2016) 187–196.
- [16] E. Ma, T. Zhu, Towards strength-ductility synergy through the design of heterogeneous nanostructures in metals, *Mater. Today* 20 (2017) 323–331.
- [17] S.W. Wu, G. Wang, Q. Wang, Y.D. Jia, J. Yi, Q.J. Zhai, J.B. Liu, B.A. Sun, H.J. Chu, J. Shen, P.K. Liaw, C.T. Liu, T.Y. Zhang, Enhancement of strength-ductility trade-off in a high-entropy alloy through a heterogeneous structure, *Acta Mater.* 165 (2019) 444–458.
- [18] X.H. An, S.D. Wu, Z.F. Zhang, R.B. Figueiredo, N. Gao, T.G. Langdon, Enhanced strength-ductility synergy in nanostructured Cu and Cu-Al alloys processed by high-pressure torsion and subsequent annealing, *Scr. Mater.* 66 (2012) 227–230.
- [19] P. Sathiyamoorthi, H.S. Kim, High-entropy alloys with heterogeneous microstructure: processing and mechanical properties, *Prog. Mater Sci.* 123 (2022) 100709.
- [20] O.N. Senkov, A.L. Pilchak, S.L. Semiatin, Effect of Cold Deformation and Annealing on the Microstructure and Tensile Properties of a HfNbTaTiZr Refractory High Entropy Alloy, *Metall. Mater. Trans. A* 49 (2018) 2876–2892.
- [21] X. Chen, J. Zhang, M. Wang, W. Wang, D. Zhao, H. Huang, Q. Zhao, X. Xu, H. Zhang, G. Huang, Research progress of heterogeneous structure magnesium alloys: a review, *J. Magnes. Alloy.* 12 (2024) 2147–2181.
- [22] Q. Ding, Y. Zhang, X. Chen, X. Fu, D. Chen, S. Chen, L. Gu, F. Wei, H. Bei, Y. Gao, M. Wen, J. Li, Z. Zhang, T. Zhu, R.O. Ritchie, Q. Yu, Tuning element distribution, structure and properties by composition in high-entropy alloys, *Nature* 574 (2019) 223–227.
- [23] Z. Wu, H. Bei, G.M. Pharr, E.P. George, Temperature dependence of the mechanical properties of equiatomic solid solution alloys with face-centered cubic crystal structures, *Acta Mater.* 81 (2014) 428–441.
- [24] E.P. George, D. Raabe, R.O. Ritchie, High-entropy alloys, *Nat. Rev. Mater.* 4 (2019) 515–534.
- [25] D.B. Miracle, O.N. Senkov, A critical review of high entropy alloys and related concepts, *Acta Mater.* 122 (2017) 448–511.
- [26] I. Basu, J.T.M. De Hosson, Strengthening mechanisms in high entropy alloys: fundamental issues, *Scr. Mater.* 187 (2020) 148–156.
- [27] H. Li, J. Wang, H. Zhi, J. Zhao, Z. Cai, M. Zhao, W.Y. Wang, J. Li, Enhancing strength-ductility synergy in L₁₂-strengthened high-entropy alloys via microband and transformation induced plasticity, *J. Mater. Sci. Technol.* 215 (2025) 86–98.
- [28] H. Li, J. Wang, Q. Xu, L. Dai, W. Liao, R. Yuan, W.Y. Wang, J. Li, High-strength medium-entropy alloy designed by precipitation-strengthening mechanism via machine learning, *Mater. Sci. Eng. A* 882 (2023) 145443.
- [29] L. Liu, Y. Zhang, J. Li, M. Fan, X. Wang, G. Wu, Z. Yang, J. Luan, Z. Jiao, C.T. Liu, P. K. Liaw, Z. Zhang, Enhanced strength-ductility synergy via novel bifunctional nano-precipitates in a high-entropy alloy, *Int. J. Plast.* 153 (2022) 103235.
- [30] F. He, Z. Yang, S. Liu, D. Chen, W. Lin, T. Yang, D. Wei, Z. Wang, J. Wang, J.-J. Kai, Strain partitioning enables excellent tensile ductility in precipitated heterogeneous high-entropy alloys with gigapascal yield strength, *Int. J. Plast.* 144 (2021) 103022.
- [31] Z. Yang, X. Liu, J. Zhao, Q. Zeng, K. Xu, Y. Li, C. Wang, L. Wang, J. Li, J. Wang, H. S. Kim, Z. Wang, F. He, Discontinuous coarsening leads to unchanged tensile properties in high-entropy alloys with different recrystallization volume fractions, *Int. J. Plast.* 176 (2024) 103963.
- [32] L. Fan, T. Yang, Y. Zhao, J. Luan, G. Zhou, H. Wang, Z. Jiao, C.T. Liu, Ultrahigh strength and ductility in newly developed materials with coherent nanolamellar architectures, *Nat. Commun.* 11 (2020) 6240.
- [33] J. Su, D. Raabe, Z. Li, Hierarchical microstructure design to tune the mechanical behavior of an interstitial TRIP-TWIP high-entropy alloy, *Acta Mater.* 163 (2019) 40–54.
- [34] C.E. Slone, J. Miao, E.P. George, M.J. Mills, Achieving ultra-high strength and ductility in equiatomic CrCoNi with partially recrystallized microstructures, *Acta Mater.* 165 (2019) 496–507.
- [35] X. Du, W. Li, H. Chang, T. Yang, G. Duan, B. Wu, J. Huang, F. Chen, C.T. Liu, W. Chuang, Y. Lu, M. Sui, E. Huang, Dual heterogeneous structures lead to ultrahigh strength and uniform ductility in a Co-Cr-Ni medium-entropy alloy, *Nat. Commun.* 11 (2020) 2390.
- [36] W. Li, T. Chou, T. Yang, W. Chuang, J.C. Huang, J. Luan, X. Zhang, X. Huo, H. Kong, Q. He, X. Du, C.-T. Liu, F.-R. Chen, Design of ultrastrong but ductile medium-entropy alloy with controlled precipitations and heterogeneous grain structures, *Appl. Mater. Today* 23 (2021) 101037.
- [37] Y. Liang, L. Wang, Y. Wen, B. Cheng, Q. Wu, T. Cao, Q. Xiao, Y. Xue, G. Sha, Y. Wang, Y. Ren, X. Li, L. Wang, F. Wang, H. Cai, High-content ductile coherent nanoprecipitates achieve ultrastrong high-entropy alloys, *Nat. Commun.* 9 (2018) 4063.
- [38] J. Fan, X. Ji, L. Fu, J. Wang, S. Ma, Y. Sun, M. Wen, A. Shan, Achieving exceptional strength-ductility synergy in a complex-concentrated alloy via architected heterogeneous grains and nano-sized precipitates, *Int. J. Plast.* 157 (2022) 103398.
- [39] S. Shukla, D. Choudhuri, T. Wang, K. Liu, R. Wheeler, S. Williams, B. Gwalani, R. S. Mishra, Hierarchical features infused heterogeneous grain structure for extraordinary strength-ductility synergy, *Mater. Res. Lett.* 6 (2018) 676–682.
- [40] T.J. Jang, W.S. Choi, D.W. Kim, G. Choi, H. Jun, A. Ferrari, F. Kormann, P.P. Choi, S.S. Sohn, Shear band-driven precipitate dispersion for ultrastrong ductile medium-entropy alloys, *Nat. Commun.* 12 (2021) 4703.
- [41] K. Ming, X. Bi, J. Wang, Precipitation strengthening of ductile Cr_{1-x}Fe₂₀Co₃₅Ni₂₀Mo₁₀ alloys, *Scr. Mater.* 137 (2017) 88–93.
- [42] P. Shi, W. Ren, T. Zheng, Z. Ren, X. Hou, J. Peng, P. Hu, Y. Gao, Y. Zhong, P. K. Liaw, Enhanced strength-ductility synergy in ultrafine-grained eutectic high-entropy alloys by inheriting microstructural lamellae, *Nat. Commun.* 10 (2019) 489.
- [43] P. Shi, Y. Zhong, Y. Li, W. Ren, T. Zheng, Z. Shen, B. Yang, J. Peng, P. Hu, Y. Zhang, P.K. Liaw, Y. Zhu, Multistage work hardening assisted by multi-type twinning in ultrafine-grained heterostructural eutectic high-entropy alloys, *Mater. Today* 41 (2020) 62–71.
- [44] Y. Xiang, J.J. Vlassak, Bauschinger effect in thin metal films, *Scr. Mater.* 53 (2005) 177–182.
- [45] X. Feaugas, On the origin of the tensile flow stress in the stainless steel AISI 316L at 300 K: back stress and effective stress, *Acta Mater.* 47 (1999) 3617–3632.
- [46] M. Yang, Y. Pan, F. Yuan, Y. Zhu, X. Wu, Back stress strengthening and strain hardening in gradient structure, *Mater. Res. Lett.* 4 (2016) 145–151.
- [47] K. Lu, A. Chauhan, F. Knöpfle, J. Aktaa, Effective and back stresses evolution upon cycling a high-entropy alloy, *Mater. Res. Lett.* 10 (2022) 369–376.
- [48] C.R. LaRosa, M. Shih, C. Varvenne, M. Ghazisaeidi, Solid solution strengthening theories of high-entropy alloys, *Mater. Charact.* 151 (2019) 310–317.
- [49] C. Zhang, C. Zhu, K. Vecchio, Non-equiatomic FeNiCoAl-based high entropy alloys with multiscale heterogeneous lamella structure for strength and ductility, *Mater. Sci. Eng. A* 743 (2019) 361–371.
- [50] C. Zhu, T. Harrington, G.T. Gray, K.S. Vecchio, Dislocation-type evolution in quasi-statically compressed polycrystalline nickel, *Acta Mater.* 155 (2018) 104–116.
- [51] D.D. Zhang, J.Y. Zhang, J. Kuang, G. Liu, J. Sun, The B₂ phase-driven microstructural heterogeneities and twinning enable ultrahigh cryogenic strength and large ductility in NiCoCr-based medium-entropy alloy, *Acta Mater.* 233 (2022) 117981.
- [52] L. Cui, S. Jiang, J. Xu, R.L. Peng, R.T. Mousavian, J. Moverare, Revealing relationships between microstructure and hardening nature of additively manufactured 316L stainless steel, *Mater. Des.* 198 (2021) 109385.
- [53] K. Ming, X. Bi, J. Wang, Realizing strength-ductility combination of coarse-grained Al_{0.2}Co_{1.5}CrFeNi_{1.5}Tl_{0.3} alloy via nano-sized, coherent precipitates, *Int. J. Plast.* 100 (2018) 177–191.
- [54] N. Yao, T. Lu, K. Feng, B. Sun, R.-Z. Wang, J. Wang, Y. Xie, P. Zhao, B. Han, X.-C. Zhang, S.-T. Tu, Ultrastrong and ductile additively manufactured precipitation-hardening medium-entropy alloy at ambient and cryogenic temperatures, *Acta Mater.* 236 (2022) 118142.
- [55] A.J. Ardell, Precipitation hardening, *Metall. Trans. A* 16A (1985) 2131–2165.
- [56] R.W. Kozar, A. Suzuki, W.W. Milligan, J.J. Schirra, M.F. Savage, T.M. Pollock, Strengthening mechanisms in polycrystalline multimodal nickel-base superalloys, *Metall. Mater. Trans. A* 40 (2009) 1588–1603.
- [57] N. Hansen, Hall-Petch relation and boundary strengthening, *Scr. Mater.* 51 (2004) 801–806.
- [58] K. Ming, X. Bi, J. Wang, Strength and ductility of CrFeCoNiMo alloy with hierarchical microstructures, *Int. J. Plast.* 113 (2019) 255–268.
- [59] J.P.H. Peter, M. Anderson, Jens Lotte, Theory of Dislocations, 3rd Ed., Cambridge University Press, New York, 2017.
- [60] B.B. He, B. Hu, H.W. Yen, G.J. Cheng, Z.K. Wang, H.W. Luo, M.X. Huang, High dislocation density-induced large ductility in deformed and partitioned steels, *Science* 357 (2017) 1029–1032.
- [61] T. Yang, Y.L. Zhao, Y. Tong, Z.B. Jiao, J. Wei, J.X. Cai, X.D. Han, D. Chen, A. Hu, J. Kai, K. Lu, Y. Liu, C.T. Liu, Multicomponent intermetallic nanoparticles and superlattice mechanical behaviors of complex alloys, *Science* 362 (2018) 933–937.
- [62] B. Gwalani, S. Dasari, A. Sharma, V. Soni, S. Shukla, A. Jagetia, P. Agrawal, R. S. Mishra, R. Banerjee, High density of strong yet deformable intermetallic nanorods leads to an excellent room temperature strength-ductility combination in a high entropy alloy, *Acta Mater.* 219 (2021) 117234.
- [63] F. He, Z. Wang, Q. Wu, D. Chen, T. Yang, J. Li, J. Wang, C.T. Liu, J. Kai, Tuning the defects in face centered cubic high entropy alloy via temperature-dependent stacking fault energy, *Scr. Mater.* 155 (2018) 134–138.
- [64] G. Chen, J.W. Qiao, Z.M. Jiao, D. Zhao, T.W. Zhang, S.G. Ma, Z.H. Wang, Strength-ductility synergy of Al_{0.1}CoCrFeNi high-entropy alloys with gradient hierarchical structures, *Scr. Mater.* 167 (2019) 95–100.
- [65] Y.L. Zhao, Y.R. Li, G.M. Yeli, J.H. Luan, S.F. Liu, W.T. Lin, D. Chen, X.J. Liu, J. Kai, C.T. Liu, T. Yang, Anomalous precipitate-size-dependent ductility in multicomponent high-entropy alloys with dense nanoscale precipitates, *Acta Mater.* 223 (2022) 117480.

- [66] Y.L. Qi, L. Zhao, X. Sun, H.X. Zong, X.D. Ding, F. Jiang, H.L. Zhang, Y.K. Wu, L. He, F. Liu, S.B. Jin, G. Sha, J. Sun, Enhanced mechanical performance of grain boundary precipitation-hardened high-entropy alloys via a phase transformation at grain boundaries, *J. Mater. Sci. Technol.* 86 (2021) 271–284.
- [67] D.G. Kim, Y.H. Jo, J. Yang, W.-M. Choi, H.S. Kim, B.-J. Lee, S.S. Sohn, S. Lee, Ultrastrong duplex high-entropy alloy with 2 GPa cryogenic strength enabled by an accelerated martensitic transformation, *Scr. Mater.* 171 (2019) 67–72.
- [68] Y. Yang, T. Chen, L. Tan, J.D. Poplawsky, K. An, Y. Wang, G.D. Samolyuk, K. Littrell, A.R. Lupini, A. Borisevich, E.P. George, Bifunctional nanoprecipitates strengthen and ductilize a medium-entropy alloy, *Nature* 595 (2021) 245–249.
- [69] J.R. Patel, M. Cohen, Criterion for the action of applied stress in the martensitic transformation, *Acta Metall.* 1 (1953) 531–538.
- [70] M. Soleimani, A. Kalhor, H. Mirzadeh, Transformation-induced plasticity (TRIP) in advanced steels: a review, *Mater. Sci. Eng. A* 795 (2020) 140023.
- [71] J. Zhang, Z. Zhao, Q. Li, J. Luan, C.-T. Liu, Y. Zhao, T. Yang, Unveiling the unique bifunctionality of $L1_2$ -structured nanoprecipitates in a FeCoNiAlTi-type high-entropy alloy, *Adv. Powder Mater.* 2 (2023) 100113.